Original Article

Visualization of Stent Lumen in MR Imaging: Relationship with Stent Design and RF Direction

Seiichiro Ohno[a,b]*, **Takashi Harimoto**[b,c], **Miyuki Hirosue**[d], **Masahiro Miyai**[e],
Kengo Hattori[b], **Masahiro Kuroda**[b], **Susumu Kanazawa**[f], **Keiji Inamura**[a], and **Hirokazu Kato**[b]

[a]Department of Radiology, Okayama University Hospital, [b]Graduate School of Health Sciences, Okayama University,
[f]Department of Radiology, Okayama University Graduate School of Medicine, Dentistry and Pharmaceutical Sciences, Okayama 700–8558, Japan,
[c]Department of Radiology, Kitagawa Hospital, Wake, Okayama 709–0451, Japan, [d]Murakami Neurosurgery Clinic,
Kasaoka, Okayama 714–0013, Japan, [e]Department of Radiology, Shimane University Hospital, Izumo, Shimane 693–8501, Japan

Magnetic resonance imaging (MRI) visualization of metallic stent lumens is possible if the stent structure counteracts eddy currents in the lumen induced by the radio frequency magnetic field, B_1. To examine the effectiveness of various stent designs in counteracting eddy currents, we anchored eight copper stent models and 2 commercially available nickel-titanium alloy (Nitinol) stents in a gel phantom, perpendicular or parallel to the direction of B_1. A mesh stent lumen showed hypointensity irrespective of its alignment relative to B_1. A solenoid stent lumen showed hypointensity with the stent axis parallel to B_1, but it had the same signal intensity as outside the lumen when perpendicular to B_1. A Moebius stent lumen showed no signal reduction, irrespective of alignment relative to B_1. Lumens of the commercially available stents showed hypointensity regardless of alignment relative to B_1. Computer simulation revealed that the signal intensities of the stents corresponded to magnetic flux densities of B_1 in the stents, which are modified by the structure of the stent. While *in vivo* MRI viewing of a Moebius stent lumen is likely possible regardless of axis alignment, inherent structural weakness may be problematic. As a more practical choice, the solenoid stent is easier to manufacture and generates no hypointensive signal when the axis is parallel to B_0.

Key words: MRI, visualization of stent lumen, solenoid pattern, Moebius pattern, direction of B_1

S tents have become indispensable tools for the treatment of vascular stenosis in the head, neck, coronary artery, and bile duct, and of various vascular diseases. X-ray computed tomography (CT) is commonly used for the assessment of restenosis, while magnetic resonance imaging (MRI) is rarely used, as it is generally considered unsuitable for confirming the therapeutic efficacy of stent implanta-tion and for lumen assessment. This is mainly because the stent lumen and surrounding area are shown as a hypointense region on MRI. Previous reports [1–4] attribute this phenomenon to radiofrequency (RF) shielding artifacts. Eddy currents, induced in a metallic stent by pulsed RF, counteract the applied RF magnetic field, obstructing the tilting of the spin axis. The magnitude of such eddy currents is depen-dent on both the composition and electrical conductiv-ity of the stent metal, as well as the stent design [1–4]. A Moebius pattern stent has been considered, as this design prevents the generation of eddy cur-

rents. Its inherent structural weakness is problematic, and thus a double-layered modified Moebius pattern stent has been proposed [5].

The aim of the present study was to devise a stent structure that minimizes the induction of eddy currents within the stent, thereby permitting improved lumen assessment. For this reason, copper was chosen as a material for the experimental stents to minimize the magnetic susceptibility artifacts.

Eight different etching patterns were applied to copper foil to produce eight stent design models, and the differences in their MRI appearances were assessed. For comparison, 2 nickel-titanium alloy (Nitinol) commercially available stents of different sizes were also evaluated.

Materials and Methods

Stent models.   Eight stent models of various patterns were produced (Figs. 1 and 2): mesh (Stent 1), solenoid (Stent 2), ring (Stent 3), Moebius (Stent 4), 1-connection and 2-connection (Stents 5 and 6, respectively), one-turn (Stent 7), and one turn with a cut (Stent 8). The configurations of Stents 5–8 were based on a spiral form to strengthen the cylindrical coil. Pattern sizes were as follows: width range: 36.0–94.0 mm; length: 50 mm; number of cycles in zigzag patterns: 12–12.5; number of rows: 20; wire width: 0.25 mm (= 0.66 points); height of zigzag patterns: 2.5 mm; peak-to-peak intervals in zigzag patterns (width): 3.00 mm; wire thickness: 1 point = 0.376 mm.

The 8 copper stents were produced by etching copper foil affixed to a flexible film. The film was a flexible photosensitive substrate consisting of polyimide (50 μm thickness) and copper foil (0.376 mm thickness) (NZ-M3K: Sunhayato Corp., Tokyo, Japan). The etched copper foil sheet was rolled and joined at the edges at the points indicated by the red dotted lines a-a' and b-b' as illustrated in Figs. 1 and 2. This resulted in a cylindrical stent model as shown in Fig. 3. To improve the stent strength, we designed Stents 5 to 8 to make the joined portion (connection between a-a' and b-b') into a spiral shape when the illustrated sheet was rolled into the cylindrical shape. The metal portions of these cylindrical forms were 11.5–11.9 mm in diameter and 50 mm long, and the edges of the film were joined using an epoxy resin adhesive (High

Super 5: Cemedine Co., Ltd., Tokyo, Japan). For Stents 1 to 3 (mesh, solenoid, and ring patterns), copper wires (0.18 mm in diameter and 2 mm long) were soldered with cream-type solder for stainless steel (SD-46: Taiyo Electric Ind. Co., Ltd., Hiroshima, Japan) to achieve electrical connection at the ends shown as red dotted lines a-a' and b-b' in Fig. 1.

The 2 commercially-available stents (Stents 9 and 10) (S.M.A.R.T.eR: Cordis Corp., Miami, FL, USA) were made of nickel-titanium alloy (Nitinol). Stent 9 was 10 mm in diameter and 60 mm long; Stent 10 was 7 mm in diameter and 43 mm long.

Human-equivalent gel phantom.   To observe the various stent models simultaneously, and to be able to change the direction of a stent axis, we used a gel phantom for the experiment instead of the commonly used liquid phantom. A 2,000-g muscle-equivalent gel phantom was prepared from the following components according to the published literature [6]:
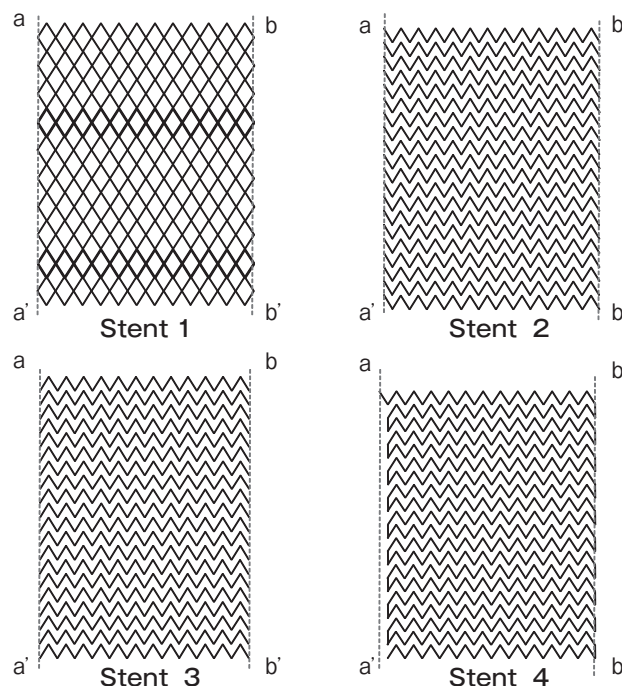

Fig. 1   Configuration of design diagrams of stent models. Stent 1: Wires form a mesh (mesh pattern). Stent 2: Wires form a coil resembling a spring shape (solenoid pattern). Stent 3: Wires form multiple rings of a single turn (ring pattern). Stent 4: Wires arranged in zigzags, alternating at every turn (Moebius pattern). Stent models are made by rolling the illustrated configurations of etched copper foil and joining red dotted lines a-a' to b-b'.
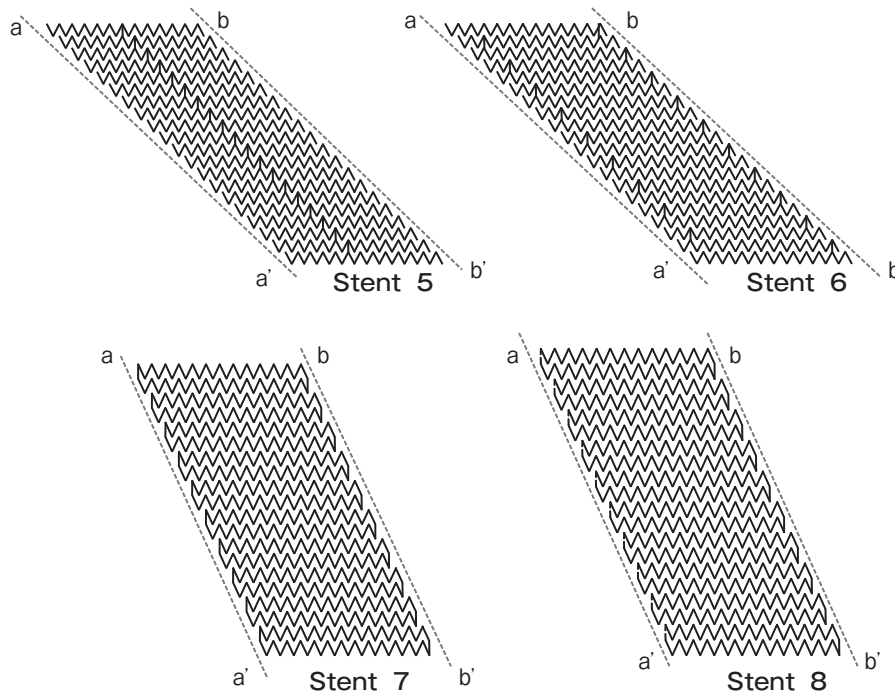
Fig. 2   Configuration of the design diagrams of stent models. Stent 5: One connection (between the upper and lower levels of zigzag patterns) in the center (1-connection pattern). Stent 6: Two connections comprising alternating upper and lower joints (on the right and left), similar to a Moebius pattern (2-connection pattern). Stent 7: A ring-shaped connection between the upper and lower layers (one-turn pattern). Stent 8: Similar to Stent 7 (one-turn pattern) but with one cut (one-turn with a cut pattern). Stent models are made by rolling the illustrated configurations of etched copper foil and joining red dotted lines a-a' to b-b'.
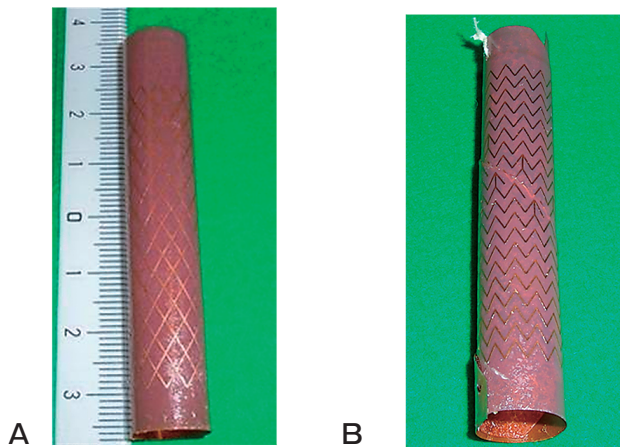

Fig. 3   Cylindrical stents made by rolling the illustrated shapes in Figs. 1 or 2. (**A**) is Stent 1 (mesh); (**B**) is Stent 6 (2-connection).

3% carrageenan (60 g), 38.7μmol/kg GdCl$_3$ (0.0204 g), 1.413% agarose (28.26 g), 0.277% NaCl (5.53 g), 0.03% NaN$_3$ (0.6 g), and 1905.59 g of water. The produced phantom had a T$_1$ value of 867 ms, a T$_2$ value of 47 ms, electrical conductivity of 0.688 S/m, and relative permittivity of 72. The ingredients were mixed in an enamel-coated porcelain container (columnar shape; diameter: 160 mm; capacity: 3 liters) and dissolved in an oil bath. While the phantom was in a liquid form, one each of the 10 types of stents was inserted into the phantom with the axes of the stents parallel to the axis of the phantom container, and then the phantom was gelled at room temperature. Placement of the stents in the phantom was done randomly. The shape of the gelled columnar phantom was 160 mm in diameter and 100 mm high.

MR imaging.   A 1.5-T MRI system (Achieva 1.5 T, Philips Medical Systems, The Netherlands) was used, and MRI was performed at a room temperature of 25 ± 1℃. A body coil installed in the MRI system was used as a transmitter coil, and an 8-channel SENSE head coil was used as a receiver coil. Stent axes were oriented in one of 2 directions by turning the gel phantom, aligning the stents axes either perpendicular or parallel to the static magnetic
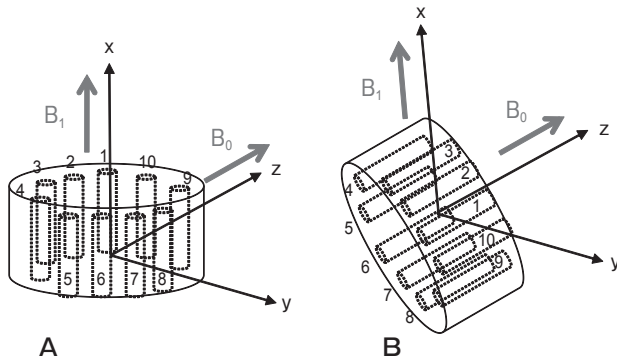
Fig. 4 Arrangement of a gel phantom containing 10 stent models aligned in the directions of the magnetostatic field (B_0) or RF (B_1). Stent models (dotted lines) are positioned either perpendicular or parallel to B_0. When B_0 is aligned to the z-axis, the direction of B_1 rotates on the x-y plane. **A**, When the stent axis is perpendicular to B_0, the direction of B_1 is parallel to the stent axis; **B**, When the stent axis is parallel to B_0, the direction of B_1 is perpendicular to the stent axis.

field (B_0), as shown in Fig. 4. When B_0 was aligned to the z-axis, B_1 rotated on the x-y plane. With the stent axis perpendicular to B_0 (Fig. 4A), B_1 was aligned parallel to the stent axis. With the stent axis parallel to B_0 (Fig. 4B), B_1 was aligned perpendicular to the stent axis. Coronal and sagittal MR images of the phantom were obtained while it was positioned as shown in Fig. 4A, as were axial and sagittal MR images with the phantom positioned as shown in Fig. 4B.

Imaging parameters for spin-echo (SE) sequences were: TR/TE, 2,000 ms/15 ms; flip angle, 90°; slice thickness, 5 mm; matrix, 256 × 256; field of view, 160 mm; number of excitations, 2; band width, 109.3 Hz/pixel; and scan time, 17 min 6 s. Those for gradient-echo (GRE) sequences were: TR/TE, 500 ms/18 ms; flip angle, 60°; slice thickness, 5 mm; matrix, 256 × 256; field of view, 160 mm; number of excitations, 2; band width, 109.3 Hz/pixel; and scan time, 4 min 17 s.

Electromagnetic field analysis. The three-dimensional magnetic flux density distribution when a stent is inserted into a rotating magnetic field was calculated using COMSOL Multiphysics (COMSOL, Inc., Stockholm, Sweden).

For the computer simulation, a copper stent model (external diameter, 10 mm; length, 25 mm) was placed in a cubic-shaped muscle model ($100 \times 100 \times 100$ mm^3;

relative permittivity: 72.27; conductivity: 0.688 S/m at 63.9 MHz). The axis passing through the centers of the upper and lower surfaces of the cubic muscle model was defined as the z-axis. The axes passing through the centers of a pair of lateral surfaces of the muscle model, which were perpendicular to the z-axis, were defined as the x-axis and y-axis, respectively. The center of the stent was set to the origin of the coordinate, and the central axis of the stent was aligned with either the x-axis or z-axis.

To provide magnetic flux density that would rotate on the x-y plane, as a boundary condition, we defined the x, y, and z components of the phasor in the upper and lower surfaces of the rectangular muscle (x-y plane) as B_{10}, $B_{10}{}^{*}\exp(-j \cdot \pi/2)$, and 0, respectively. The x, y, and z components of the phasor in the lateral surfaces of the rectangular muscle y-z plane were defined as 0, $B_{10}{}^{*}\exp(-j \cdot \pi/2)$, and 0, respectively, and the x, y, and z components of the phasor in the lateral surfaces of the rectangular muscle z-x plane were defined as B_{10}, 0, and 0, respectively, where $B_{10} = 2.934 \times 10^{-6}$ T.

Results

MR images of the 10 stents
1. Coronal and axial MR images of the 10 stents obtained by SE or GRE sequence

Fig. 5 shows MR images of the 10 different types of stent using SE or GRE sequence. In Figs. 5A and 5B, the stents were oriented perpendicular to B_0 with B_1 parallel to the stent axes. In Fig. 5C and 5D, the stents were oriented parallel to B_0 with B_1 perpendicular to the stent axes. Signal distributions over the phantom were homogeneous except inside the stent, because the signal profiles across the phantom in 2 perpendicular directions in Figs. 5(A)–(D) were homogeneous.

With SE sequences, as shown in Figs. 5A and 5C, the lumens of Stents 1, 9, and 10 showed very low signal intensity. The lumens of Stents 4, 5, 6, 7, and 8 showed the same signal intensity as the area outside the lumens. Stents 2 and 3 in Fig. 5A showed mildly lower signal intensities in the stent lumens than those outside the lumens, while in Fig. 5C the signals were of equal intensity in and outside the stent lumens.

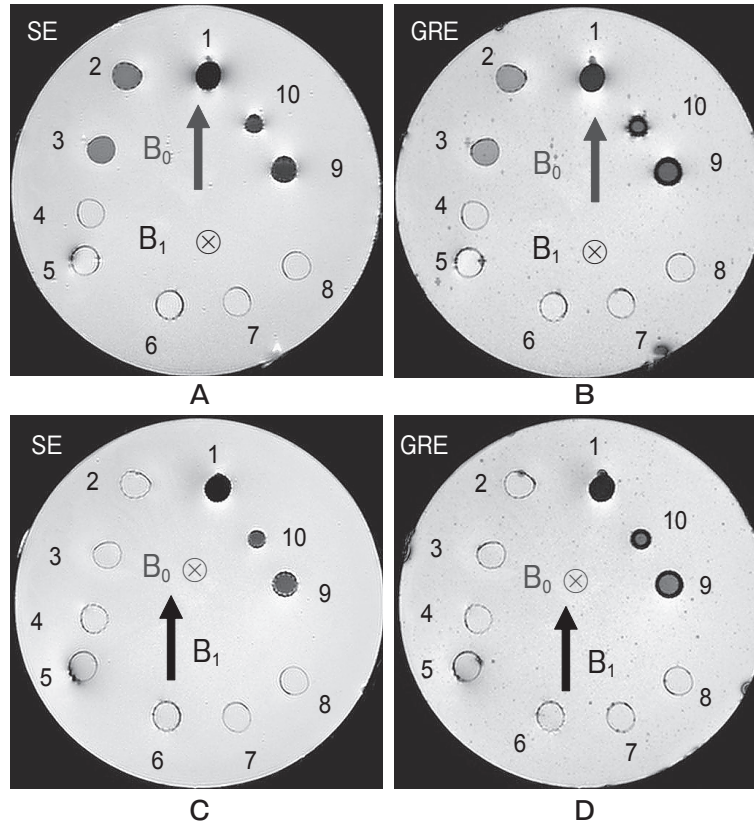GRE sequences as shown in Figs. 5B and 5D had

Fig. 5   Coronal and axial MR images of a phantom containing 8 stent models and two Nitinol stents. **A**, SE MR image showing the stent axes parallel to B_1.; **B**, GRE MR image showing the stent axes parallel to B_1.; **C**, SE MR image showing the stent axes perpendicular to B_1.; **D**, GRE MR image showing the stent axes perpendicular to B_1.

tendencies similar to those of the SE sequences, though the contours of Stents 9 and 10 were depicted as thicker than in the SE sequences.

2. Sagittal MR images of 3 stents obtained by SE sequence

Of the 10 stent models shown in Fig. 5, 3 of the stent patterns were analyzed: Stent 1 (mesh pattern), in which eddy currents could be induced irrespective of B_1 direction; Stent 2 (solenoid pattern), in which eddy currents could be induced depending on B_1 direction; and Stent 4 (Moebius pattern), in which an eddy current could not be induced irrespective of the B_1 direction. Fig. 6 contains sagittal MR images of Stents 1 (mesh), 2 (solenoid), and 4 (Moebius) obtained by SE sequence. Fig. 6A shows the MR images of the Fig. 4A configurations, with B_1 parallel to the stent axes. Fig. 6B shows the MR images of the Fig. 4B configurations, with B_1 perpendicular to the stent axes.

The Stent 1 (mesh pattern) lumen showed very low signal intensity, irrespective of the direction of B_1. The Stent 2 (solenoid pattern) lumen had mildly low signal intensity when the stent axis was parallel to B_1, but the same signal intensity as that outside the lumen when the stent axis was perpendicular to B_1. The Stent 4 (Moebius pattern) lumen showed the same signal intensity as the area outside the lumen, regardless of the B_1 direction.

3. MR images of 3 stents obtained by GRE sequence

Fig. 7 contains sagittal MR images of Stents 1, 2, and 4 obtained by GRE sequence. Fig. 7A shows the MR images of the Fig. 4A configurations, with B_1 parallel to the stent axes. Fig. 7B shows the MR images of the Fig. 4B configurations, with B_1 perpendicular to the stent axes.

The Stent 1 (mesh) lumen showed very low signal intensity, irrespective of the B_1 direction. The Stent
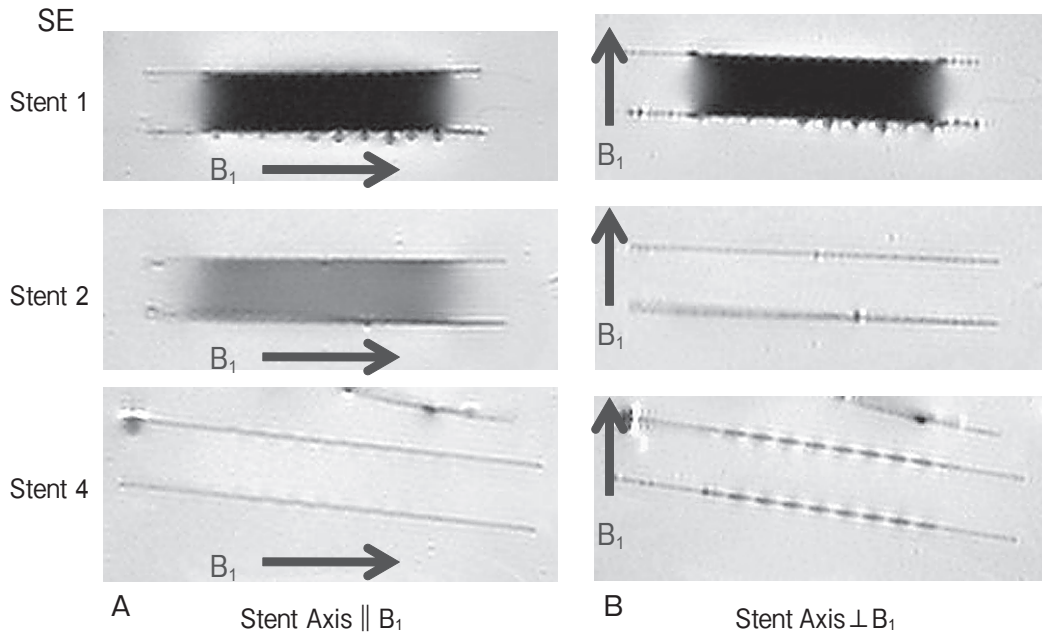
Fig. 6   Sagittal SE MR images of Stent 1 (mesh pattern), Stent 2 (solenoid pattern), and Stent 4 (Moebius pattern). **A**, The stent axes are parallel to B_1.; **B**, The stent axes are perpendicular to B_1.
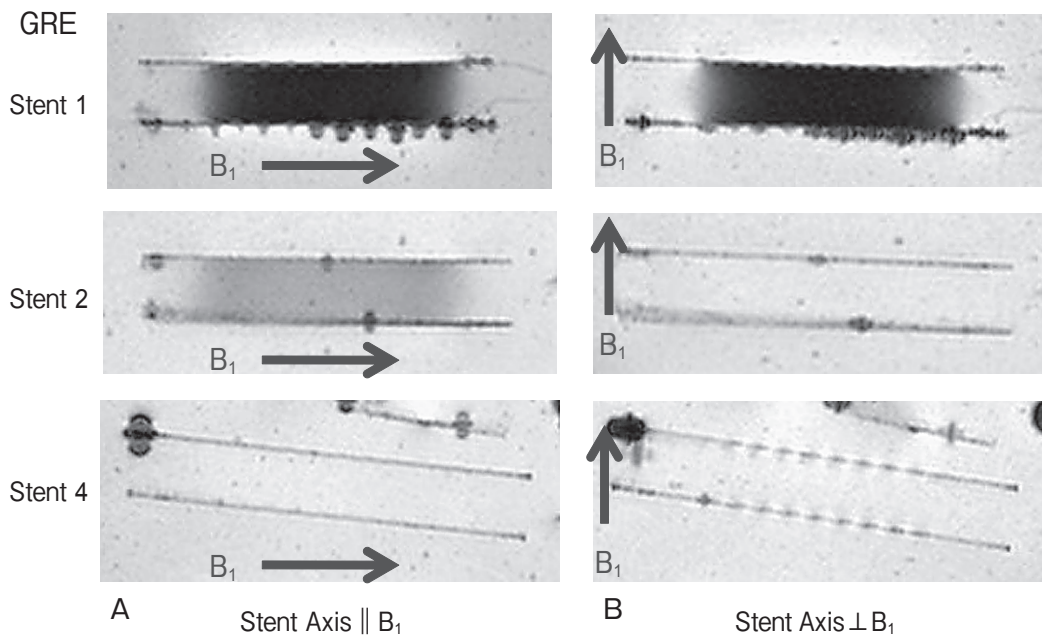

Fig. 7   Sagittal GRE MR images of Stent 1 (mesh pattern), Stent 2 (solenoid pattern), and Stent 4 (Moebius pattern). **A**, The stent axes are parallel to B_1.; **B**, The stent axes are perpendicular to B_1.

2 (solenoid) lumen had mildly low signal intensity when the stent axis was parallel to B_1, but it had the same intensity as the area outside the lumen when the stent axis was perpendicular to B_1. The Stent 4 (Moebius) lumen showed the same signal intensity as the area outside the lumen, regardless of the B_1 direction.

Computational models and results. Computed illustrations of Stents 1, 2, and 4 are shown in Fig. 8A. Figs. 8B and 8C show the distributions of RF magnetic flux density on the z-x plane at $y = 0$ when the direction of B_1 rotates on the x-y plane. The B_1 arrow indicates the direction of magnetic flux density at a certain instant. The central axis of the stent in Fig. 8B coincides with the x-axis; that in Fig. 8C coincides with the z-axis. The arrows in the figures represent the vectors of the magnetic flux density at the moment that the direction of B_1 turns to $+$ x-axis. As shown in Figs. 8B and 8C, the lumen of the mesh pattern stent exhibits reduced magnetic flux density irrespective of the direction of B_1. The solenoid pattern stent lumen shows reduced magnetic flux density when the stent axis is parallel to B_1, but no such reduction when the stent axis is perpendicular to B_1. The lumen of the Moebius pattern stent exhibits no reduction of magnetic flux density regardless of the direction of B_1.
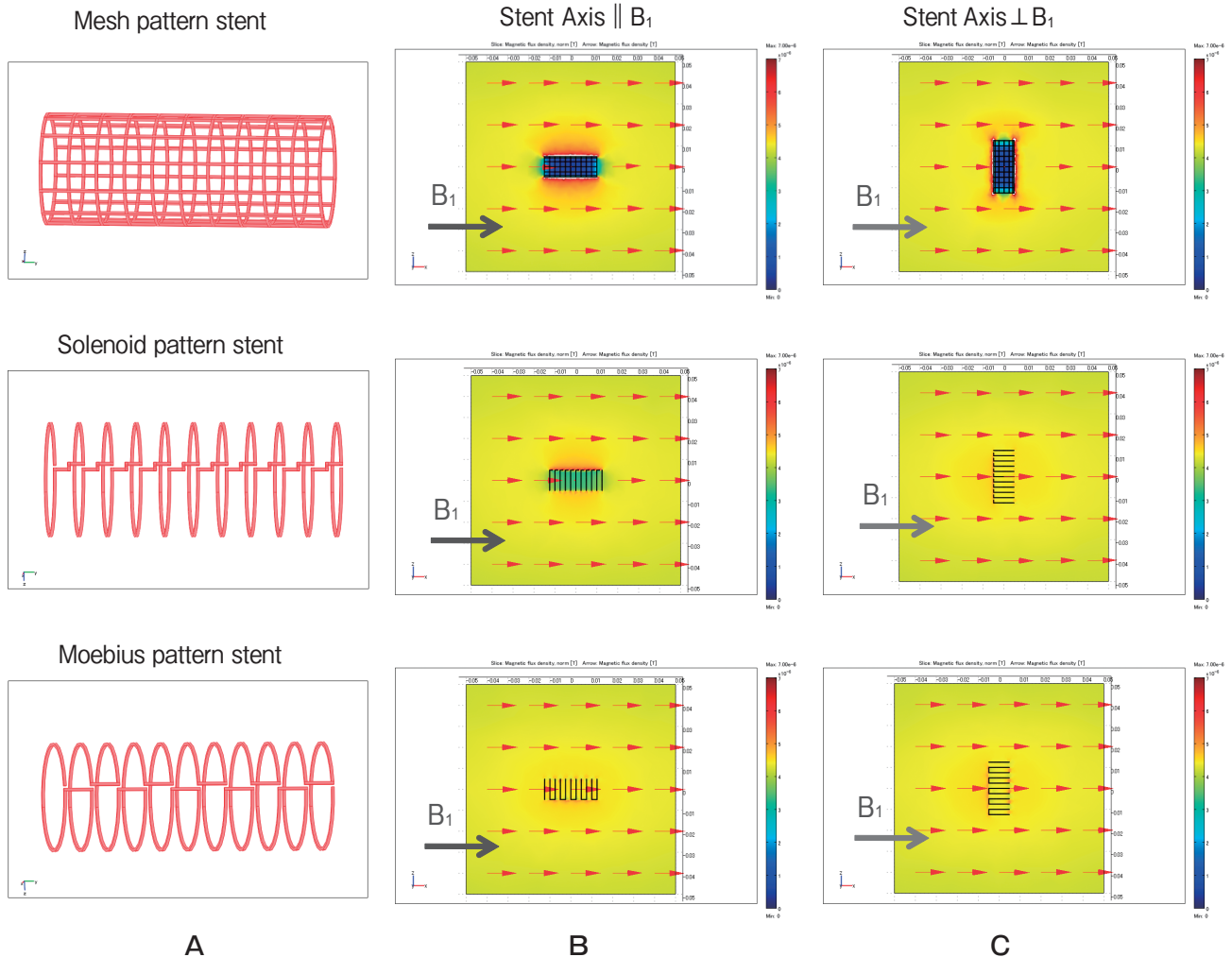

Fig. 8 Computed magnetic flux density distribution in mesh, solenoid, and Moebius pattern stents. **A**, Illustrations showing the schema of the mesh pattern stent (top left), solenoid pattern stent (middle left), and Moebius pattern stent (bottom left); **B**, Magnetic flux distributions with the stent axes parallel to B_1.; **C**, Magnetic flux distributions with the stent axes perpendicular to B_1.

Comparison of signal intensities in the lumen with B_1 directions in experiments. As shown in Fig. 5, the lumens of Stents 1, 9, and 10 showed very low signal intensity in both SE and GRE sequences, regardless of whether B_1 was parallel or perpendicular to the stent axes. The lumens of Stents 4 to 8 showed the same signal intensity as the area outside the lumen with both SE and GRE sequences, regardless of whether B_1 was parallel or perpendicular to the stent axes. Stents 2 and 3 exhibited mildly low signal intensities in the lumens with both SE and GRE sequences when B_1 was parallel to the stent axes, but the signal intensities in the lumens were the same as those in the areas outside the lumens when B_1 was perpendicular to the stent axes.

Comparison of experimental stents and simulation model computations. There was a correlation between the signal intensities of 3 types of stent (Stent 1–mesh, Stent 2–solenoid, and Stent 4–Moebius) as depicted in Figs. 6 and 7, and the magnetic flux densities of the RF magnetic fields, *i.e.*, B_1 (Fig. 8).

1. Mesh stent: The Stent 1 (mesh) lumen exhibited very low signal intensity whether the stent axis was parallel or perpendicular to B_1, and the computation showed low magnetic flux density in the stent lumen.

2. Solenoid stent: The Stent 2 (solenoid) lumen showed mildly low signal intensity when the stent axis was parallel to B_1, and computation showed low magnetic flux density in the stent lumen. However, when the experimental stent axis was perpendicular to B_1, the lumen had the same signal intensity as the area outside the lumen, and computation showed no reduced magnetic flux density in the stent lumen.

3. Moebius stent: The Stent 4 (Moebius) lumen signal intensity inside the stent did not decrease, regardless of whether the stent axis was parallel or perpendicular to B_1, and computations showed no reduced magnetic flux density in the stent lumen.

Discussion

The ability to perform MRI assessment of a stent lumen without use of a contrast agent would be advantageous and serve to reduce the element of invasiveness to patients. In the present study we evaluated the visualization of a stent lumen by MRI using 8 types of copper prototype experimental stents produced by etching technique and 2 nickel-titanium alloy (Nitinol) commercially available stents. Artifacts produced by stents consist of those caused by magnetic susceptibility and RF shielding [1–4]. RF shielding artifacts arise in proportion to electrical conductivity [2]. Copper is a highly conductive and diamagnetic material that minimizes magnetic susceptibility artifacts, making it an optimal material for the present study.

Our study confirmed that RF shielding artifacts occur relative to the stent structure. Further, stent lumen assessment was shown to be feasible if the numerous closed loops of the stent wires are positioned so as to not interact with the RF magnetic fields (Stent 3 in Fig. 1), or when the stent wires form a Moebius pattern (Stent 4 in Fig. 1) that induce induction currents in the reverse directions at adjacent wire parts (as described in the patent document) [5]. However, the Moebius pattern stent is vulnerable to deformation and must be reinforced with an insulating material or overlapped structure [5].

Stents are generally categorized as either wire-coil or tube stents. The former consist of metal wires wound into a stent configuration. These wire-coil stents have weak mechanical strength due to a lack of supporting structures and have a high probability of restenosis, and thus they are generally not used for intravascular treatment [7]. Tube stents are commonly made of Nitinol and are produced by a cutting laser from Nitinol tubing [8]. These stents have excellent mechanical strength, and their structure helps to prevent vascular restenosis [7]. The nickel-titanium shape-memory alloy is used in many types of stents [9–11] and is characterized by its low magnetic susceptibility [1, 12] and excellent elastic properties [10]. Stents 9 and 10 in our study were commercially available and made of Nitinol. Both stents had a mesh pattern, consisting of multiple rings and connecting wires. Eddy currents readily flow within the mesh structure of this type of stent, resulting in poor visualization of the interior of the stents.

Many studies have focused on methods of improving the visualization of the stent lumen. Bartels *et al.* [12] showed the relationship between B_0, magnetic susceptibility, and RF shielding based on their results using commercially available stents. They noted a reduction of artifacts when a stent was placed parallel to B_0 and proposed an increase of the nominal flip angle to improve lumen visualization. Buecker *et al.*

[13] developed a stent using the non-inductive winding method. The lumen of such a stent inserted in the renal artery was visualized with no stent artifacts. Quick *et al.* [14] proposed a compensation method for reduced B_1 in which the intensity of B_1 in the stent is amplified by a resonant circuit composed of a solenoid pattern stent and an added capacitor. Stent material with low electrical conductivity allows better visualization of the solenoid stent lumen due to the minimizing of the eddy currents induced by RF magnetic fields. Carbon fiber has an electrical conductivity of $7.27 \times 10^4 \mathrm{S/m}$, approximately $1/1{,}000$ that of copper, and Graf *et al.* [4] reported that a carbon-fiber solenoid stent model, with the stent axis positioned parallel to B_1, showed no reduction of signals using a 1.5-T MRI system.

Another method of visualizing a stent lumen centers on shaping the stent structure to counteract induction currents, such as the Moebius pattern [5]. The present study showed that visualization of a Moebius pattern stent lumen is possible, irrespective of the direction of the stent axis relative to the direction of B_1 (Stent 4 in Fig. 5). However, this structure is inherently weak and presents manufacturing difficulties. In contrast, the structure of a solenoid is highly elastic, and solenoid-pattern stents have been used in animal experiments [15, 16]. With placement of the solenoid-pattern stent perpendicular to B_1, an evaluation of a stent lumen commonly done by CT examination would then be possible by MRI examination. In this case, angiography without contrast media can be expected.

In conclusion, the present study has shown that visualization of a solenoid pattern stent lumen is possible when the alignment of the stent axis is perpendicular to B_1. As the positioning of many luminal organs, including the cervical artery, aorta, arteries of the lower limbs, and bile duct, is parallel to B_0 in the case of ordinary MRI systems, it appears that the solenoid stent structure is the preferable option to allow visualization of a stent lumen.

References

1. Bartels LW, Bakker CJ and Viergever MA: Improved lumen visualization in metallic vascular implants by reducing RF artifacts. Magn Reson Med (2002) 47: 171–180.
2. Wang Y, Truong TN, Yen C, Bilecen D, Watts R, Trost DW and Prince MR: Quantitative evaluation of susceptibility and shielding effects of Nitinol, Platinum, Cobalt-alloy, and Stainless steel stents. Magn Reson Med (2003) 49: 972–976.
3. van Holten J, Wielopolski P, Bruck E, Pattynama PM and van Dijk LC: High flip angle imaging of metallic stents: implications for MR angiography and intraluminal signal interpretation. Magn Reson Med (2003) 50: 879–883.
4. Graf H, Steidle G, Lauer UA and Schick F: rf enhancement and shielding in MRI caused by conductive implants: dependence on electrical parameters for a tube model. Med Phys (2005) 32: 337–342.
5. Gregorich D: Overlapped stents for scaffolding, flexibility and MRI compatibility. Patent Application Publication: Boston US 2005/0278019 A1, USA (2005).
6. Kato H, Kuroda M, Yoshimura K, Yoshida A, Hanamoto K, Kawasaki S, Shibuya K and Kanazawa S: Composition of MRI phantom equivalent to human tissues. Med Phys (2005) 32: 3199–3208.
7. Morton AC, Crossman D and Gunn J: The influence of physical stent parameters upon restenosis. Pathol Biol (Paris) (2004) 52: 196–205.
8. Raval A, Choubey A, Engineer C and Kothwala D: Development and assessment of 316LVM cardiovascular stents. Materials Science and Engineering (2004) 386: 331–343.
9. Whitcher FD: Simulation of in vivo loading conditions of Nitinol vascular stent structures. Computers & Structures (1997) 64: 1005–1011.
10. Liu X, Wang Y, Yang D and Qi M: The effect of ageing treatment on shape-setting and superelasticity of a nitinol stent. Materials Characterization (2008) 59: 402–406.
11. Wu W, Qi M, Liu XP, Yang DZ and Wang WQ: Delivery and release of nitinol stent in carotid artery and their interactions: A finite element analysis. Journal Biomech (2007) 40: 3034–3040.
12. Bartels LW, Smits HF, Bakker CJ and Viergever MA: MR imaging of vascular stents: effects of susceptibility, flow, and radiofrequency eddy currents. J Vasc Interv Radiol (2001) 12: 365–371.
13. Buecker A, Spuentrup E, Ruebben A and Günther RW: Artifact-free in-stent lumen visualization by standard magnetic resonance angiography using a new metallic magnetic resonance imaging stent. Circulation (2002) 105: 1772–1775.
14. Quick HH, Kuehl H, Kaiser G, Bosk S, Debatin JF and Ladd ME: Inductively coupled stent antennas in MRI. Magn Reson Med (2002) 48: 781–790.
15. Dotter CT, Buschmann RW, McKinney MK and Rosch J: Transluminal expandable Nitinol coil stent grafting: preliminary report. Radiology (1983) 147: 259–260.
16. Cragg A, Lund G, Rysavy J, Castaneda F, Castaneda-Zuniga W and Anplatz K: Nonsurgical placement of arterial endoprostheses: a new tequnique using Nitinol wire. Radiology (1983) 147: 261–263.